THE JOURNAL OF PHYSICAL CHEMISTRY C

Article

pubs.acs.org/JPCC

Adsorption of Chain Molecules in Slit-Shaped Pores: Development of a SAFT-FMT-DFT Approach

Bryan J. Schindler, Lucas A. Mitchell, Clare McCabe, Peter T. Cummings, and M. Douglas LeVan*

Department of Chemical and Biomolecular Engineering, Vanderbilt University, 2301 Vanderbilt Place, Nashville, Tennessee 37235, United States

ABSTRACT: Density functional theory (DFT) is commonly used to treat the adsorption of molecules in carbon and silica pores of various geometries. In this work, we develop a DFT with an accurate molecular-based equation of state to calculate thermodynamic properties using fundamental measure theory (FMT), which is a rigorous approach for the treatment of homogeneous and nonhomogeneous hard-sphere fluids. A theoretical framework results with adsorbing molecules treated as hard-sphere chains with square-well attractive interactions. The Mansoori−Carnahan−Starling−Leland and Carnahan−Starling−Boublik equations of state are used for the hard-sphere interactions, and a version of the statistical associating fluid theory for potentials of variable range (SAFT-VR) is used to describe the square-well fluid. First- and second-order perturbative attractive terms are included in the theory. Theoretical predictions are in good agreement with published results for Monte Carlo simulations of the adsorption of chain molecules. In an extension to published studies, the impact of potentials of increasing complexity are compared using square-well and Lennard−Jones wall potentials. For more realistic adsorption of molecules of varying chain length, full slit-shaped pores are modeled using a 10−4 wall potential. The new approach provides accurate predictions of adsorption of chain molecules in model systems. It should be useful for predicting adsorption on flat surfaces and in slit-shaped pores as well as for analyzing experimental data.

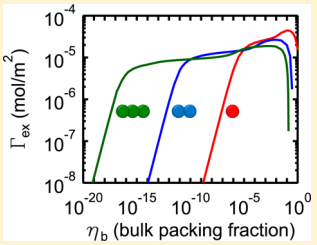

1. INTRODUCTION

Use of molecular simulation, development of accurate models, and comparison of theoretical predictions with experimental results help to advance our understanding of adsorption and its application. The introduction of density functional theory (DFT) to model inhomogeneous fluids represented a significant advance toward understanding confined fluid behavior and was encouraged by the desire to model a variety of phase transitions accurately.

Many versions of classical DFT have been proposed to calculate the thermodynamic properties of systems of varying complexity. In an early treatment, Tarazona[1,2] introduced a weighted density approximation for spherical molecules in which a power series expansion in density was used to describe the direct correlation function. This approach has been applied to many problems in adsorption.[3−10] Our development is based instead on the application of fundamental measure theory.

Fundamental measure theory (FMT) was developed by Rosenfeld[11,12] and later improved upon by Roth et al.[13] as an extension of scaled particle theory for inhomogeneous fluids. However, Roth's advancement of FMT could not satisfy one of the central equations of the Rosenfeld FMT; specifically, the theory was not consistent with the scaled particle theory differential equation in the bulk.[14,15] This led to an improvement by Hansen-Goos and Roth,[14] which corrected the inconsistency. FMT uses simple geometric factors that describe the direct correlation function and has been used for a variety of applications in phase transitions[6,16] and adsorption.[6,16−19] Reviews[15,20,21] of the development of DFT for spherical molecules are available for both the weighted density approximation and FMT. Evans[21] elaborates on the success of incorporating Rosenfeld's FMT into a DFT, including for mixtures of hard spheres.

There is much interest in expanding the use of DFT to systems of more complex molecules, such as chain fluids and polymers. In order to predict the properties of such molecules, the pioneering work by Wertheim[22−25] on thermodynamic perturbation theory has been utilized by several groups to develop combined statistical associating fluid theory (SAFT)-DFT approaches.

In the SAFT approach, a fluid is described by a chain of tangentially bonded monomer segments that interact via dispersion and association sites. The free energy is obtained from a sum of the different contributions that account for the monomer−monomer interaction, chain formation, and intermolecular association. Since the SAFT EOS has a firm basis in statistical mechanical perturbation theory for well-defined molecular models, systematic improvement (e.g., by improved expressions for the monomer free energy and structure) and extension of the theory (e.g., by considering new monomer fluids, bonding schemes and association interactions) is possible by comparing the theoretical predictions with computer simulation results on the same molecular model.[26−29] Due to its role in improving and validating the theory, the importance of having an underlying molecular model in contrast to engineering equations of state cannot be overemphasized. In comparing with experimental data, it is important to be aware of the error inherent in the theory, as

Received: July 3, 2013
Revised: September 11, 2013
Published: September 16, 2013

revealed by comparison with computer simulation results, before attempting to estimate the intermolecular parameters. This invaluable advantage over empirical EOSs has resulted in many extensions and variations of the original SAFT expressions, which essentially correspond to different choices for the monomer fluid and different theoretical approaches to the calculation of the monomer free energy and structure. The simplest SAFT approach describes associating chains of hard-sphere segments with the dispersion interactions described at the mean-field level (SAFT-HS).[30,31] At a similar level of theory is the most extensively applied version of SAFT, that of Huang and Radosz (SAFT-HR),[32] which has been used to correlate the phase behavior of a wide range of fluid systems. Comparisons with SAFT-HR are often provided when a new version of SAFT is developed to demonstrate the improved ability of the new equation; however, direct and meaningful comparisons between the more recent "second-generation" SAFT equations (namely, soft-SAFT,[33,34] SAFT-VR,[35] and PC-SAFT[36]) are more rare. From the limited number of studies that have performed such comparisons, it is clear that any one version is not superior over the others in general terms.[37−42] A recent review by McCabe and Galindo[43] provides a thorough discussion of the various forms of SAFT and the many systems to which they have been applied. Of particular relevance to this work is SAFT-VR,[35] which keeps a more formal link with the molecular model than other versions of SAFT and as such can be more easily rigorously extended to study more complex molecular models.[44−47] SAFT-VR has been applied to the study the phase behavior of a wide range of fluids, though of particular relevance to the current work are the studies of short alkanes through to polymers.[26,27,39,48−50]

Several molecular theory-based equations of state, including multiple versions of SAFT, have been combined with DFT using modified versions of Rosenfeld's FMT. Among those most relevant to this work, Yethiraj and Woodward[51] and Forsman and Woodward[52] developed a DFT for square-well chains in hard-wall slit pores. Their approach combined the generalized Flory equation of state with a DFT based on a weighted density approximation for the free energy functional. Jackson and co-workers[53,54] developed a SAFT-based DFT by combining SAFT-HS[30,31] with a local density approximation to model the vapor−liquid interface of associating fluids. Only qualitative agreement with experimental surface tension data was found, and in subsequent work, SAFT-HS was replaced by the SAFT-VR equation resulting in more accurate predictions of the surface tension due to the more accurate description of the bulk properties.[55−59] Yu and Wu[60,61] and Yu et al.[62] combined the first-order thermodynamic perturbation theory of Wertheim[22,23] for hard-sphere chains with a modified version of Rosenfeld's FMT to predict the adsorption behavior of mixtures of hard polymeric fluids. Bryk et al.[63] later combined Roth's version of FMT and SAFT for tangentially bonded Lennard−Jones (LJ) chains to study the vapor−liquid interface of associating LJ chains as well as their adsorption in slit pores. Ye et al.[64,65] used SAFT-VR as the input to a DFT similar to that of Yethiraj and Woodward[51] to describe chain molecules and attractive wall potentials inside slit pores. Chapman and co-workers developed interfacial SAFT (iSAFT) by combining a DFT based on Rosenfeld's FMT for monomers with bulk fluid properties obtained from a mean-field level SAFT to model bulk and interfacial adsorption properties.[66,67]

In this paper, we extend the theory of Yu and Wu[61] to treat adsorption on flat surfaces and in slit-shaped pores. We develop a DFT using a modified version of Rosenfeld's FMT and a version of SAFT based on SAFT-VR to treat the adsorption of confined chain molecules. For the chain fluids, we use a perturbation analysis for attractive terms out to second order, rather than assume a mean field. We compare our results with Monte Carlo simulations of hard-sphere chains near hard walls and chains with attractive potentials in the presence of hard walls and attractive walls. We then compare results for attractive chains in slit pores with a square-well attractive wall potential and a Lennard−Jones attractive wall potential. Finally, we use the theory to predict density profiles in full pores with interactions described by a 10−4 potential.

2. THEORY

The treatment developed here constructs a DFT using a version of SAFT based on the SAFT-VR approach for the bulk fluid thermodynamics.[35] The DFT is implemented for inhomogeneous fluids near plane walls and flat pore walls through introduction of FMT for hard-sphere and hard-sphere chain interactions to permit the use of SAFT to describe the attractive potential. In doing so, SAFT is transformed from a method for the treatment of a homogeneous fluid in the bulk to a method for analysis of an inhomogeneous fluid near a surface. First- and second-order perturbation terms for the attractive potential originate in SAFT-VR, but it is necessary to recast them for the inhomogeneous fluid. Below we outline the main expressions of the SAFT-FMT-DFT approach developed for confined and bulk fluids and provide additional details in the Appendix.

Density functional theory is used to calculate the density profile that minimizes the grand potential function $\Omega[\rho_m(\mathbf{R})]$, where $\rho_m(\mathbf{R})$ is the density profile of a chain molecule as a function of segment position, i.e., $\mathbf{R} \equiv (\mathbf{r}_1, \mathbf{r}_2,...,\mathbf{r}_m)$, and m is the number of segments in the chain. Minimization is performed by setting the functional derivative of the grand potential with respect to density equal to zero to obtain $\rho_m(\mathbf{R})$. The grand potential is calculated from

$$\Omega[\rho_m(\mathbf{R})] = F[\rho_m(\mathbf{R})] + \int \rho_m(\mathbf{R})[V_{\text{ext}}(\mathbf{R}) - \mu]\mathrm{d}\mathbf{R} \quad (1)$$

where $F[\rho_m(\mathbf{R})]$ is the Helmholtz free energy, μ is the chemical potential for the chain molecule calculated from a version of the SAFT-VR equation of state in the bulk (see appendix), and $V_{\text{ext}}(\mathbf{R})$ is the external potential.

The Helmholtz free energy is calculated from an ideal term and excess terms. In the general formulation of SAFT, the excess terms describe hard-sphere repulsion, attractive interactions, and chain connectivity. Since we are incorporating both first- and second-order perturbation terms, we write the Helmholtz free energy and the chemical potential as

$$F = F_{\text{id}} + F_{\text{hs}} + F_1 + F_2 + F_{\text{chain}} \quad (2)$$

$$\mu = \mu_{\text{id}} + \mu_{\text{hs}} + \mu_1 + \mu_2 + \mu_{\text{chain}} \quad (3)$$

where the terms correspond to the ideal, hard-sphere, first-order attractive, second-order attractive, and chain contributions, respectively.

The ideal term is calculated by

$$F_{\text{id}} = kT \int \rho(\mathbf{r})[\ln(\Lambda^3\rho(\mathbf{r})) - 1]\mathrm{d}\mathbf{r} \quad (4)$$

where Λ is the de Broglie wavelength. The segment density $\rho(\mathbf{r})$ is used instead of $\rho_m(\mathbf{R})$ because we are solving for the

segment density, not the molecular density. The chemical potential contribution of the ideal term is calculated from

$$\mu_{\mathrm{id}} = kT \ln(\rho_{m,b}\Lambda^3) \tag{5}$$

where $\rho_{m,b}$ is the molecular number density, which is equal to ρ_b/m, where ρ_b is the bulk segment number density.

The hard-sphere term is calculated in FMT using a series of four scalar and two vector densities, which are defined by

$$n_i(\mathbf{r}) = \int \rho(\mathbf{r}')\omega_i(\mathbf{r}-\mathbf{r}')\mathrm{d}\mathbf{r}' \tag{6}$$

where the subscript (i = 0, 2, 3, $V1$, $V2$) denotes the weighting function. The six weighting functions are related to the geometry of a molecule and are

$$\omega_0(r) = \frac{\omega_2(r)}{4\pi R^2} \tag{7}$$

$$\omega_1(r) = \frac{\omega_2(r)}{4\pi R} \tag{8}$$

$$\omega_2(r) = |\nabla\Theta(R-r)| = \delta(R-r) \tag{9}$$

$$\omega_3(r) = \Theta(R-r) \tag{10}$$

$$\omega_{V1}(\mathbf{r}) = \frac{\omega_{V2}(\mathbf{r})}{4\pi R} \tag{11}$$

$$\omega_{V2}(\mathbf{r}) = \nabla\Theta(R-r) = \frac{\mathbf{r}}{r}\delta(R-r) \tag{12}$$

for a sphere of radius R, where Θ is the Heaviside step function and δ is the Dirac delta function. The vector terms $\mathbf{n}_{V1}$ and $\mathbf{n}_{V2}$ vanish in the bulk.

The contribution of the hard-sphere repulsive term to the free energy is calculated in FMT using[13−15]

$$F_{\mathrm{hs}} = kT \int \Phi^{\mathrm{hs}}[n_\alpha(\mathbf{r}')]\mathrm{d}\mathbf{r}' \tag{13}$$

In the original "White Bear" version of FMT by Roth et al.,[13] a Mansoori−Carnahan−Starling−Leland (MCSL) fluid, which is described by an equation of state for hard-sphere mixtures that reduces to the Carnahan−Starling equation of state[68] for single components, was used to give

$$\Phi^{\mathrm{hs}}[n_\alpha(\mathbf{r})] = -n_0\ln(1-n_3) + \frac{n_1n_2 - \mathbf{n}_{V1}\cdot\mathbf{n}_{V2}}{1-n_3} + \frac{(n_2^3 - 3n_2\mathbf{n}_{V2}\cdot\mathbf{n}_{V2})(n_3 + (1-n_3)^2\ln(1-n_3))}{36\pi n_3^2(1-n_3)^2} \tag{14}$$

The more recent "White Bear Mark II" revision of FMT by Hansen-Goos and Roth[14] corresponds to a Carnahan−Starling−Boublík (CSB) fluid and is of the form

$$\Phi^{\mathrm{hs}}[n_\alpha(\mathbf{r})] = -n_0\ln(1-n_3) + (n_1n_2 - \mathbf{n}_{V1}\cdot\mathbf{n}_{V2})\times\frac{1+\frac{1}{3}\phi_2(n_3)}{1-n_3} + (n_2^3 - 3n_2\mathbf{n}_{V2}\cdot\mathbf{n}_{V2})\times\frac{1-\frac{1}{3}\phi_3(n_3)}{24\pi(1-n_3)^2} \tag{15}$$

with

$$\phi_2(n_3) = \frac{1}{n_3}[2n_3 - n_3^2 + 2(1-n_3)\ln(1-n_3)] \tag{16}$$

and

$$\phi_3(n_3) = \frac{1}{n_3^2}[2n_3 - 3n_3^2 + 2n_3^3 + 2(1-n_3)^2\ln(1-n_3)] \tag{17}$$

The chemical potential contribution for the hard-sphere term is calculated from

$$\mu_{\mathrm{hs}} = mkT\sum_i \frac{\partial\Phi_b^{\mathrm{hs}}}{\partial n_{i,b}}\frac{\partial n_{i,b}}{\partial\rho_b} \tag{18}$$

where in the bulk $n_{0,b} = \rho_b$, $n_{1,b} = R\rho_b$, $n_{2,b} = 4\pi R^2\rho_b$, and $n_{3,b} = (4/3)\pi R^3\rho_b$.

For the attractive terms, a perturbation analysis[35] gives for the first-order term

$$F_1 = \frac{1}{2}\int\rho(\mathbf{r}')\int\rho(\mathbf{r}'')g^{\mathrm{hs}}[n_3(\mathbf{r}'');\,\mathbf{r}'']\phi(|\mathbf{r}'-\mathbf{r}''|)\mathrm{d}\mathbf{r}''\mathrm{d}\mathbf{r}' \tag{19}$$

in which the attractive potential is the square-well given by

$$\phi(r) = \begin{cases} -\varepsilon_{ff} & \text{if} \quad \sigma_{ff} \le r < \lambda_f\sigma_{ff} \\ 0 & \text{if} \quad r \ge \lambda_f\sigma_{ff} \end{cases} \tag{20}$$

where $\sigma_{ff} = 2R$ is the hard-sphere diameter, and the hard-sphere radial distribution function, $g^{\mathrm{hs}}[n_3(\mathbf{r});\mathbf{r}]$, developed by Chang and Sandler[69] with a Verlet−Weis[70] correction, is a function of density and distance. The chemical potential contribution for the first-order term is

$$\mu_1 = -4m\varepsilon(\lambda_f^3 - 1)\left(2n_{3,b}g_e^{\mathrm{hs}} + n_{3,b}^2\frac{\partial g_e^{\mathrm{hs}}}{\partial\eta_e}\frac{\partial\eta_e}{\partial n_{3,b}}\right) \tag{21}$$

where, following Gil-Villegas et al.[35] for SAFT-VR, the hard-sphere radial distribution function at contact is calculated using the Carnahan−Starling[68] expression

$$g_e^{\mathrm{hs}} = \frac{1-\eta_e/2}{(1-\eta_e)^3} \tag{22}$$

The effective density η_e is calculated for an extended value up to $\lambda_f = 3$ using the relation of Patel et al.[71]

$$\eta_e = \frac{c_1n_{3,b} + c_2n_{3,b}^2}{(1+c_3n_{3,b})^3} \tag{23}$$

with

$$\begin{pmatrix} c_1 \\ c_2 \\ c_3 \end{pmatrix} = \begin{pmatrix} -3.165 & 13.35 & -14.81 & 5.703 \\ 43.00 & -191.7 & 273.9 & -128.9 \\ 65.04 & -266.5 & 361.0 & 162.7 \end{pmatrix}\begin{pmatrix} 1/\lambda_f \\ 1/\lambda_f^2 \\ 1/\lambda_f^3 \\ 1/\lambda_f^4 \end{pmatrix} \tag{24}$$

The second-order attractive term adopted here is an improvement on the treatment of Barker and Henderson,[72,73] which was used in SAFT-VR. Developed by Zhang[74] and based on a macroscopic compressibility approximation that takes the correlation of molecules in neighboring shells into account, it is given by

dx.doi.org/10.1021/jp406572d | J. Phys. Chem. C 2013, 117, 21337−21350

$$F_2 = -\frac{1}{4kT}\int\rho(\mathbf{r}')\int\rho(\mathbf{r}'')(1+2\xi{n_3}^2) \times [\phi(|\mathbf{r}'-\mathbf{r}''|)]^2 K^{hs}(\mathbf{r}'')g^{hs}[n_3(\mathbf{r}'');\mathbf{r}'']\mathrm{d}\mathbf{r}''\mathrm{d}\mathbf{r}' \quad (25)$$

where $\xi = 1/{\eta_{con}}^2$ with $\eta_{con} = 0.493$, which is the packing fraction where the fluid condenses.[74] The hard-sphere isothermal compressibility for a CSB fluid is calculated from

$$K^{hs} = \frac{(1-n_3)^4}{1+4n_3+4{n_3}^2-4{n_3}^3+{n_3}^4} \quad (26)$$

The chemical potential contribution for the second-order attractive term is given by

$$\mu_2 = \frac{-2m\varepsilon^2(\lambda_f^3-1)}{kT}\{4\xi{n_{3,b}}^3K^{hs}{g_e}^{hs} + (1+2\xi{n_{3,b}}^2) \times \left[2n_{3,b}K^{hs}{g_e}^{hs} + {n_{3,b}}^2\left(\frac{\partial K^{hs}}{\partial n_{3,b}}{g_e}^{hs} + K^{hs}\frac{\partial {g_e}^{hs}}{\partial\eta_e}\frac{\partial\eta_e}{\partial n_{3,b}}\right)\right]\} \quad (27)$$

For the hard-sphere chain term, Yu and Wu[61] recast Wertheim's first-order perturbation theory for chain connectivity in a bulk fluid to a form needed for an inhomogeneous fluid using the weighted densities of FMT. The chain contribution to the Helmholtz energy is described by

$$F_{chain} = kT\int\Phi^{chain}[n_\alpha(\mathbf{r}')]\mathrm{d}\mathbf{r}' \quad (28)$$

$$\Phi^{chain}[n_\alpha(\mathbf{r})] = \frac{1-m}{m}n_0\zeta\ln y^{hs}(\sigma_{ff}, n_\alpha) \quad (29)$$

$$\zeta = 1 - \frac{\mathbf{n}_{V2}\cdot\mathbf{n}_{V2}}{n_2^2} \quad (30)$$

$$y^{hs}(\sigma_{ff}, n_\alpha) = \frac{1}{1-n_3} + \frac{n_2\sigma_{ff}\zeta}{4(1-n_3)^2} + \frac{{n_2}^2{\sigma_{ff}}^2\zeta}{72(1-n_3)^3} \quad (31)$$

where y^{hs} is the contact value of the cavity correlation function between segments. Note that, following Yu and Wu,[61] Φ_{chain} differs from the SAFT-VR term, which would contain the square-well (y^{sw}) rather than the hard-sphere (y^{hs}) cavity correlation function. The chemical potential contribution for the chain term is given by

$$\mu_{chain} = kT(1-m)\sum_i\frac{\partial\Phi_b^{chain}}{\partial n_i}\frac{\partial n_i}{\partial\rho_b} \quad (32)$$

The equation used for the external potential depends on the situation being described. The interaction between a hard-sphere chain and a hard wall is described by

$$V_{ext}(z) = \begin{cases} 0, & z \geq 0 \\ \infty, & z < 0 \end{cases} \quad (33)$$

The interaction with a square-well attractive wall is given by

$$V_{ext}(z) = \begin{cases} 0, & z > \lambda_w\sigma_{sf} \\ -\varepsilon_w, & 0 < z < \lambda_w\sigma_{sf} \\ \infty, & z < 0 \end{cases} \quad (34)$$

where σ_{sf} is the solid–fluid collision diameter. The interaction with a Lennard–Jones attractive wall is represented as

$$V_{ext}(z) = 4\varepsilon_w\left[\left(\frac{\sigma_{sf}}{z}\right)^{12} - \left(\frac{\sigma_{sf}}{z}\right)^6\right] \quad (35)$$

To compare the square-well and Lennard–Jones attractive walls, the ε values were determined by equating the second virial coefficient[75] of the square-well wall, B_{SW}, to the second virial coefficient of the Lennard–Jones wall, B_{LJ}, holding σ_{sf} constant.

Integrating the 6–12 Lennard–Jones potential over the walls, rather than applying it to a slice of a pore, gives the 10–4 wall potential on each side of the pore described by[76,77]

$$V_{ext}(z) = \phi_w(z) + \phi_w(H-z) \quad (36)$$

with

$$\phi_w(z) = 2\pi\varepsilon_w\rho_w{\sigma_{sf}}^2\left[\frac{2}{5}\left(\frac{\sigma_{sf}}{z}\right)^{10} - \left(\frac{\sigma_{sf}}{z}\right)^4\right] \quad (37)$$

where ρ_w is the density of the wall molecules.

Taking the functional derivative of eq 1 and rearranging the result gives the following equation for calculation of the segment equilibrium density profile[61]

$$\rho(z) = \frac{1}{\Lambda^3}\exp(\mu)\sum_{i=1}^{m}\exp\left[-\frac{\psi(z)}{kT}\right]G^i(z)G^{m+1-i}(z) \quad (38)$$

where μ is the chemical potential. The solution method involves iterating on the segment density. In eq 38 we have

$$\psi(z) = \frac{\delta F_{hs}}{\delta\rho(\mathbf{r})} + \frac{\delta F_1}{\delta\rho(\mathbf{r})} + \frac{\delta F_2}{\delta\rho(\mathbf{r})} + \frac{\delta F_{chain}}{\delta\rho(\mathbf{r})} + V_{ext} \quad (39)$$

and

$$G^i = \int\exp\left[-\frac{\psi(z)}{kT}\right]\frac{\Theta(\sigma_{ff}-|z-z'|)}{2\sigma_{ff}}G^{i-1}\,\mathrm{d}z' \quad (40)$$

where $G^1(z) = 1$. We note that due to the summation term in eq 38, the number of segments m in the implementation of SAFT is limited to integer values.

The equilibrium value of the density, calculated from eq 38, can be used to calculate the average density in a pore from

$$\rho_{avg}(H,P) = \frac{1}{m}\frac{1}{H}\int_0^H\rho(z)\mathrm{d}z \quad (41)$$

where H is the pore width. The surface excess is then given by

$$\Gamma_{ex} = (\rho_{avg} - \rho_{m,b})H \quad (42)$$

3. RESULTS AND DISCUSSION

First, we compare predictions of density profiles for adsorption of chain molecules on flat surfaces with several published results of Monte Carlo simulations; in doing so, we also assess the magnitudes of the contributions of the terms in eqs 2 and 3 on the density profiles. Second, we extend a published study using its parameters to consider adsorption in narrow pores with the fluid–wall potential given by the square-well potential, and we compare results with those for a Lennard–Jones wall potential. Finally, we consider adsorption in a slit-shaped pore with the fluid–wall potential given by the 10–4 potential.

Adsorption on Flat Surfaces and Comparisons with Monte Carlo Simulations. Predictions from our theoretical approach using the FMT formulations of both Roth et al.[13] and

dx.doi.org/10.1021/jp406572d | J. Phys. Chem. C 2013, 117, 21337–21350

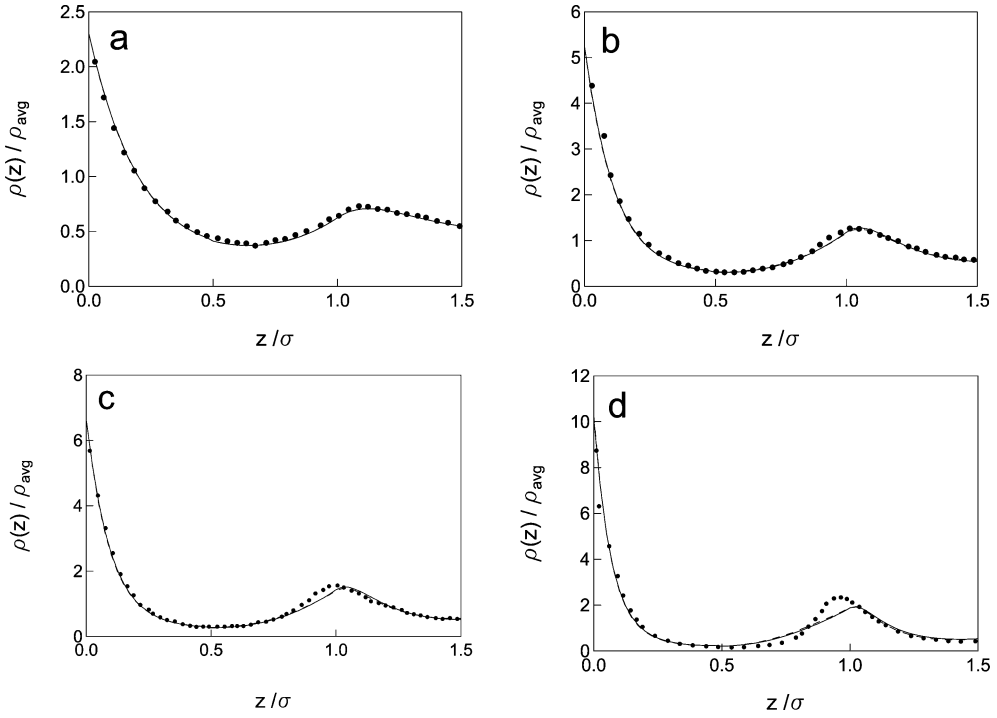

Figure 1. Hard sphere against a hard wall at bulk packing fractions η_b of (a) 0.57, (b) 0.755, (c) 0.81, and (d) 0.91. Circles are Monte Carlo results,[78] solid curve is White Bear FMT, and dashed curve is White Bear Mark II FMT.

Hansen-Goos and Roth[14,15] are compared here with a variety of different Monte Carlo simulations from the literature. First considered are hard spheres against hard walls. Then, a set of hard-sphere chains against hard walls is treated to establish the validity of the chain function. Next, attractive potentials are incorporated to compare results with simulations for hard and attractive walls. In our figures for these comparisons we follow the common convention of measuring the pore wall coordinate from the inside edge of the pore.

For hard spheres against hard walls, we set $m = 1$, $\varepsilon_{ff} = 0$, and $V_{ext} = \infty$. Figure 1 shows density profiles compared with data of Snook and Henderson[78] for hard spheres against hard walls at four bulk densities from $\rho\sigma_{ff}^3 = 0.57$ to 0.91. The results agree with the well-known requirement for momentum transfer that the density of any fluid in contact with a hard wall is $\rho(0) = P/kT$. All of the figures show good quantitative agreement between our approach and the Monte Carlo simulations. Only slight differences are seen at the highest densities in Figure 1c and 1d.

Figure 1 also shows our calculations comparing the use of the White Bear FMT[13] and the White Bear Mark II FMT.[14,15] The density profiles from Figure 1c for both formulations are shown in an expanded form in Figure 2. The White Bear Mark II FMT agrees more closely with the Monte Carlo simulations of Snook and Henderson[78] for hard spheres against hard walls. The insert in Figure 2 shows a further blown-up portion of where the two theories differ the most. These differences are apparent in modeling chain molecules as well, with White Bear Mark II producing the closest fitting curves. For this reason and because, as mentioned earlier, the derivation of the White Bear Mark II FMT is consistent with scaled-particle theory in the bulk,[14] all of the following calculations reported in this paper use the White Bear Mark II FMT.

For hard-sphere chains and hard walls, several comparisons were performed involving adsorption of m-mers. This was done

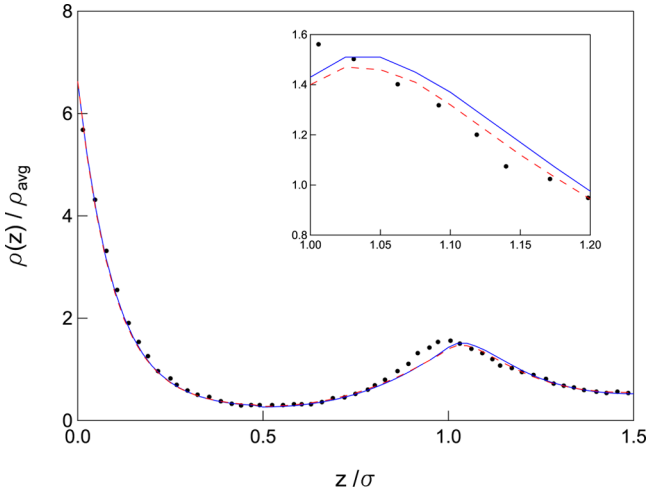

Figure 2. Hard sphere against a hard wall at a bulk packing fraction of $\eta_b = 0.81$. Circles are Monte Carlo results,[78] solid curve is the White Bear FMT, and dashed curve is the White Bear Mark II FMT.

by setting m equal to the number of spherical monomer units in the chain. Figure 3 compares segment density profiles determined using our approach with a series of Monte Carlo simulations by Kierlik and Rosinberg[79] for 3-mer chains. Predictions show excellent agreement in both values and structure over the full range of bulk packing fractions, from $\eta_b = 0.1$ to 0.45. At the lower densities in Figure 3a and 3b, the density at contact is lower than the average density and increases to form the first layer; however, a layer near $z/\sigma_{ff} = 1$ is still apparent. For the intermediate densities shown in Figure 3c and 3d, the density at contact is above the average density, as for hard spheres, and shows the first layer becoming better defined. For the higher densities shown in Figure 3e and 3f, the second layer has begun to form.

dx.doi.org/10.1021/jp406572d | J. Phys. Chem. C 2013, 117, 21337−21350

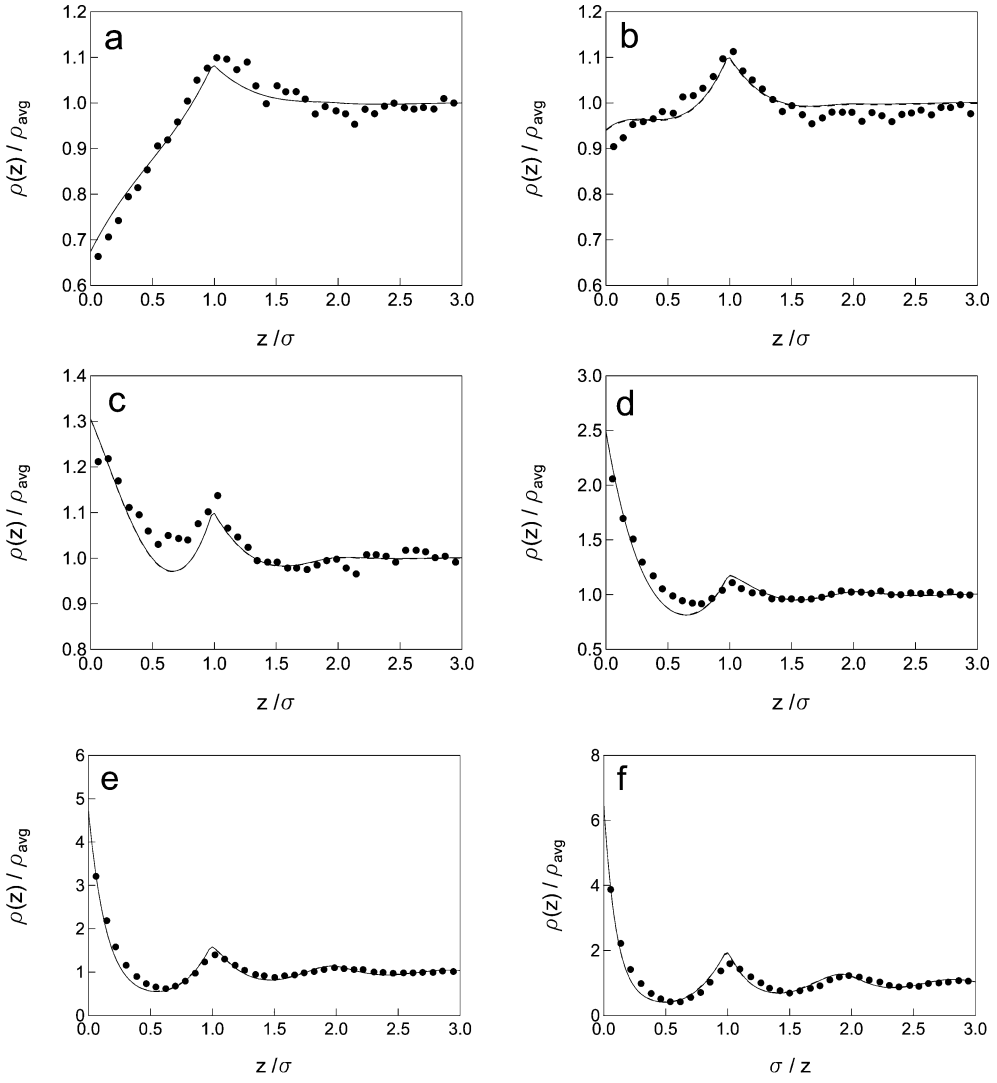

Figure 3. Hard-sphere 3-mer against a hard wall at bulk packing fractions η_b of (a) 0.1, (b) 0.15, (c) 0.20, (d) 0.30, (e) 0.40, and (f) 0.45. Circles are Monte Carlo results,[79] and solid curve is the White Bear Mark II FMT.

Considering longer hard-sphere chains, Figure 4 shows a comparison of our predicted segment density profiles with simulations of 4-mer chains by Dickman and Hall[80] at bulk packing densities from 0.107 to 0.417. The density profiles show good agreement with the density at the wall and with the maximum and minimum values. Figure 5 shows our predictions compared with simulations of 20-mer chains by Yethiraj and Woodward[51] at bulk packing fractions from 0.1 to 0.35. Small deviations between the theoretical predictions and the Monte Carlo simulations are apparent. Figure 5a shows a slightly lower segment density in the center of the pore, and the maximum and minimum values in the troughs and peaks show some variation with the Monte Carlo results in Figure 5b and 5c. However, the structure of the theory agrees well, showing minima and maxima at the correct locations. Thus, it is apparent from Figures 1−5 that the theory provides generally good agreement with Monte Carlo simulation results over a wide range of bulk densities and chain lengths.

We now consider an attractive potential incorporated into the model by the inclusion of eqs 19 and 25. Results are compared with the Monte Carlo simulations of Ye et al.,[64] which use $\varepsilon_{ff}/kT = 3.0$, $\lambda_f = 1.5$, and $\lambda_w = 1.0$. The interaction with the hard wall was treated using eq 33. Figure 6 shows the density profiles of 3-mers with second-order attractive potentials against a hard wall. Figure 6a, for a bulk packing fraction η_b of 0.10, shows good agreement with the Monte Carlo simulations. We note distinct differences between Figure 6a and Figure 3a resulting from application of the attractive potential; specifically, the density at contact is lower with the attractive potential included and does not show the peak at $z/\sigma_{ff} = 1$. For $\eta_b = 0.3$, Figure 6b shows good agreement in the placement of the maximum and minimum of the density profile; however, significantly larger oscillations are apparent in comparison with the results of the Monte Carlo simulation or in comparison with the hard-sphere chain results shown in Figure 3d.

For an attractive square-well wall, we use eq 34 and compare the predictions or our approach with the Monte Carlo simulation results of Ye et al.,[64] which use $\varepsilon_w/kT = -1.0$. Our predictions show good qualitative agreement with the simulations. Figure 7a shows the density profile for $\eta_b = 0.10$. The contact density is somewhat lower than for the Monte Carlo simulations, but the density profile shows the same general trends. The drop at $z/\sigma_{ff} = 1$ as well as the hump between $z/\sigma_{ff} = 1$ and 2 are properly located. The results for $\eta_b = 0.3$ are shown in Figure 7b. Our approach shows good

dx.doi.org/10.1021/jp406572d | J. Phys. Chem. C 2013, 117, 21337−21350

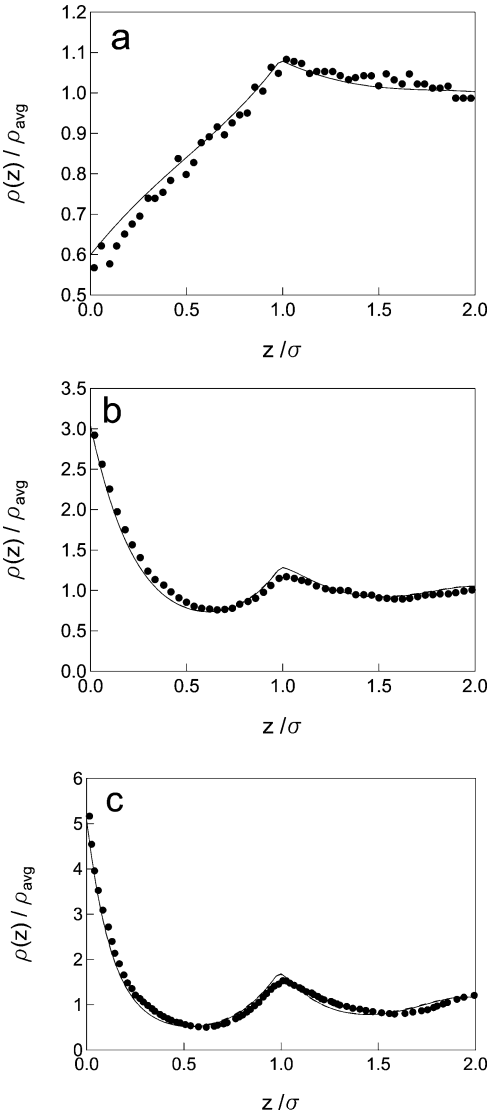

Figure 4. Hard-sphere 4-mer against a hard wall at bulk packing fractions η_b of (a) 0.107, (b) 0.340, and (c) 0.417. Circles are Monte Carlo results,[80] and solid curve is the White Bear Mark II FMT.

quantitative agreement with the Monte Carlo simulation, such as the sharp density decrease at $z/\sigma_{ff} = 1$. When compared to the results for the hard wall shown in Figure 6, differences are apparent. The attractive potential of the wall clearly affects the profiles. Where the attractive potential ends at $z/\sigma_{ff} = 1$ there is the sharp decrease, which is not seen for the hard wall. Also, the densities near the wall are higher for the attractive wall, and the oscillations toward the center of the pore are dampened.

In comparing the impacts of the various terms in eqs 2 and 3 on the density profiles, we found that the effect of the first-order attractive term was an order of magnitude less than the hard-sphere and chain terms. Similarly, the impact of the second-order attractive term was an order of magnitude less than the first-order attractive term.

Extensions of Literature Examples. To consider further the impact of the attractive potential, pores were modeled with attractive walls simulated using the square-well potential of eq 34 and, for comparison, the Lennard–Jones potential of eq 35. We retain the parameter values from Ye et al.[64] for the attractive wall with the square-well potential. The value of ε for the Lennard–Jones wall potential was obtained from the square-well wall parameters of Ye et al. by equating second virial coefficients while holding σ_{sf} constant. The coordinate system is shown in Figure 8, where the two potentials are compared. For the square-well and LJ pores, the pore width was measured from the edge of the wall atoms of one wall to the edge of the wall atoms of the opposite wall. The coordinate inside the pore was measured from the edge of the pore wall to the center of a chain segment.

Pore density profiles for 3-mers with second-order attractive potentials inside a square-well attractive pore are shown in Figure 9 at a packing fraction of $\eta_b = 0.30$ for increasing pore widths from $1\sigma_{ff}$ to $8\sigma_{ff}$. For the larger pore widths studied, the density profile of Figure 7b is reproduced from each pore wall. Oscillations at the center of the $8\sigma_{ff}$ pore are of much lower amplitude than those of the smaller pores. The effects of the wall interations are short ranged, and so the center of the larger pores is not influenced by the wall potential. This leads to the center of the larger pores having a lower density than near the wall, approaching the bulk value of $\rho\sigma_{ff}^3 = 0.57$. As the pores become narrower, the oscillations become less and less pronounced until the pore is less than $2\sigma_{ff}$ wide. At a pore width less than $2\sigma_{ff}$, because the wall potential extends $1\sigma_{ff}$ from each wall, the attractive potentials from both walls begin to overlap. Steric effects in the small pores do not allow the molecules to form separate layers until, at a width of $1\sigma_{ff}$, a single layer of molecules is formed.

Similar behavior is apparent in Figure 10, where the attractive wall is determined by the Lennard–Jones potential. Comparing the integer pore widths, the SW wall predictions are similar to those of the LJ wall. The peaks and troughs coincide for the two potentials, although the oscillations are more prominent in the center of the large pores of Figure 10 as the LJ potential is much farther reaching. In pores between adjacent integer values of σ_{ff} (e.g., Figure 10b–d), formation of another layer of molecules can be observed. A noticeable difference between the two potentials occurs at $1.5\sigma_{ff}$ away from each wall, where the SW potential becomes zero, resulting in a sharp decrease in the density seen previously in Figures 7 and 9g–i. This occurs only in pores larger than $3\sigma_{ff}$, for which the potentials from each wall no longer overlap, leaving a region inside the pore with only fluid–fluid interactions. Another difference is that the density begins to change closer to the LJ wall. Because the LJ potential is a soft potential, it does not produce any of the sharp increases or decreases in the density profile found for the SW wall. The LJ potential produces a smoother profile at the walls but also broadens the width of the peak, as shown in Figures 9a and 10a.

As the pore size increases, the influence of the pore walls on the molecules located near the pore center decreases, as would be expected. In the $8\sigma_{ff}$ pore, the wall potential exerts very little influence at the center. From Figure 8, the LJ potential extends approximately $2\sigma_{ff}$ from each wall, so pores larger than about $6\sigma_{ff}$ will have very little influence of the pore walls in the center of the pore. For these large pores, the same oscillations occur near each wall of every pore, consistent with molecules adsorbing on a single flat wall rather than within a pore.

Adsorption in Slit-Shaped Pores. To consider more realistic adsorption in slit-shaped pores, whole pores were modeled with attractive walls using the 10–4 potential[76,77] of eq 37. A comparison of the LJ and 10–4 wall potentials is shown in Figure 11. The 10–4 potential is much more attractive than the LJ potential, since the 10–4 potential allows for the walls to extend from a single-atom wall (as in the SW and LJ cases) to a continuous wall one layer of atoms thick.

dx.doi.org/10.1021/jp406572d | J. Phys. Chem. C 2013, 117, 21337–21350

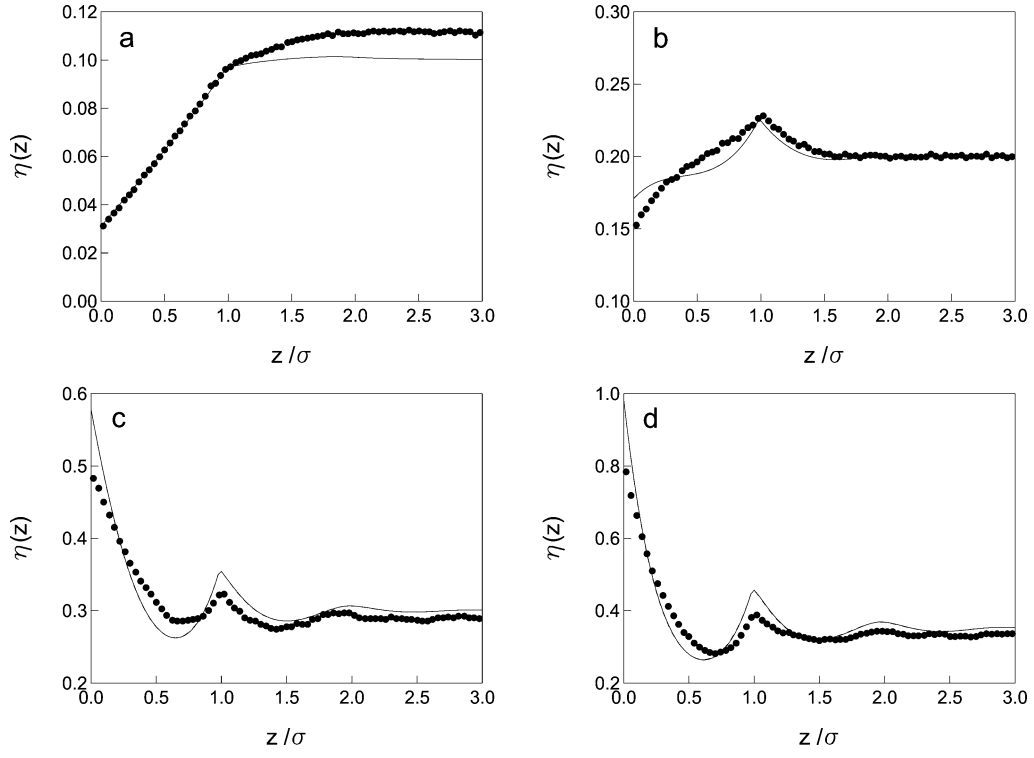

Figure 5. Hard-sphere 20-mer against a hard wall at bulk packing fractions η_b of (a) 0.10, (b) 0.20, (c) 0.30, and (d) 0.35. $\eta(z) \equiv \rho(z)\sigma_{ff}^3(\pi/6)$ is the local packing fraction in the pore. Circles are Monte Carlo results,[51] and solid curve is the White Bear Mark II FMT.

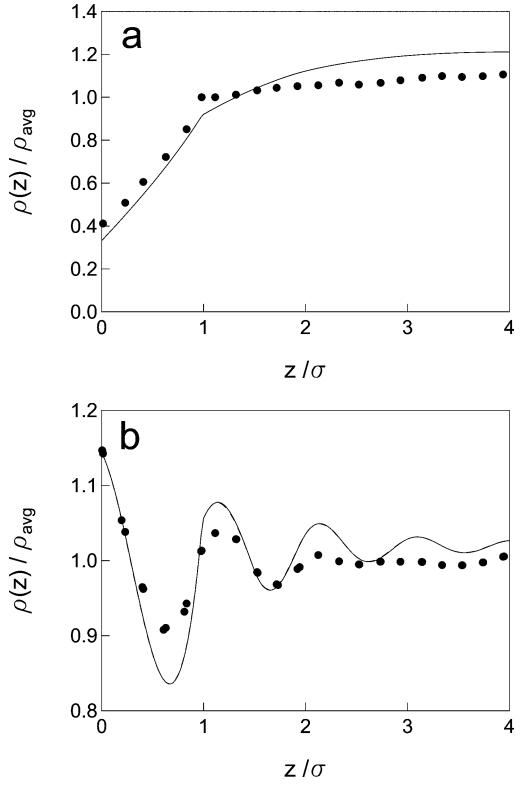

Figure 6. Attractive 3-mer against a hard wall at bulk packing fractions η_b of (a) 0.10 and (b) 0.30. Circles are Monte Carlo results,[64] and solid curve is the White Bear Mark II FMT.

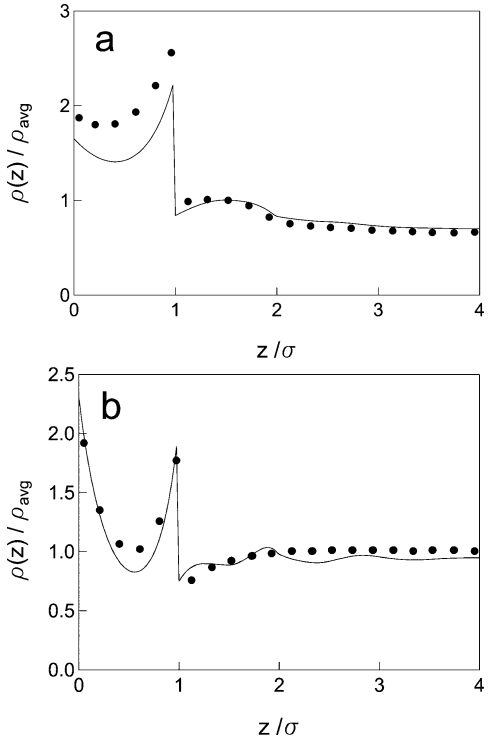

Figure 7. Attractive 3-mer against an attractive SW wall at bulk packing fractions η_b of (a) 0.10 and (b) 0.30. Potential between the wall and the fluid is $\varepsilon_w/kT = -1.0$. Circles are Monte Carlo results,[64] and solid curve is the White Bear Mark II FMT.

This allows the 10−4 potential to extend father from the wall into the pore in comparison to the LJ potential, as shown in Figure 11. The 10−4 potential used in this theory is similar in depth to other well-known potentials in the literature.[76]

dx.doi.org/10.1021/jp406572d | J. Phys. Chem. C 2013, 117, 21337−21350

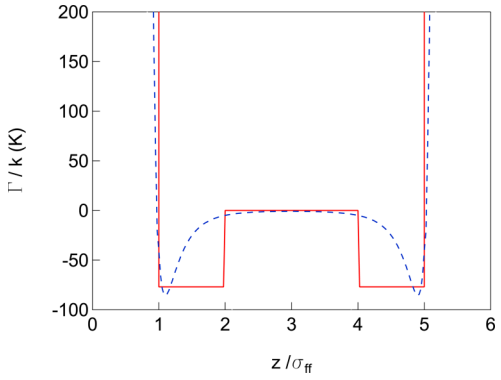

Figure 8. Square-well and Lennard–Jones wall potentials for attractive walls. Solid curve is square-well potential, and dashed curve is Lennard–Jones 6–12 potential.

Pore density profiles for 3-mers against 10–4 walls are shown in Figure 12. Pore densities for the continuous wall are much larger than for the single-wall atom LJ case shown in Figure 10 due to many more wall atoms interacting with the chain molecules. Also, the density peaks are much steeper for 10–4 walls due to the greater attraction of the chain molecules to the walls and formation of more distinct layers. Furthermore, the density between peaks for the 10–4 walls approaches zero, which is significantly different from the SW or LJ wall where the wall attractive potentials are not as strong. It should be noted that the density profiles for the $2\sigma_{ff}$ and $3\sigma_{ff}$ pores are narrower than the other pores with 10–4 walls. Also, the peaks in the density profiles for these pores are much higher than those of the other pores. This results from the two walls of the pore exerting strong overlapping attractive potentials with the molecules inside the pore at small pore widths. As the pores becomes wider, the potentials become weaker as the attraction by the far wall, now further away, lessens. Thus, the molecules in the pore do not adsorb as strongly in the center as the pore widens past $3\sigma_{ff}$. At a pore width of $8\sigma_{ff}$, the density at the center of the pore has approached the bulk density.

The effect of chain length was also considered. Figure 13 shows isotherms for a 3-mer, 2-mer, and 1-mer in a $4\sigma_{ff}$ pore. Surface excess, calculated using eq 42, is plotted versus bulk packing fraction. The 1-mer pore isotherm becomes nonlinear at a bulk packing fraction of approximately 10^{-6}. A point is reached where the average density within the pore increases more slowly than the bulk density and the surface excess begins to decrease. The 2-mer chain has similar transitions, with the surface excess passing through zero at a bulk packing fraction of 0.2. The 3-mer chain has the broadest isotherm, with the average pore density dropping below the bulk density at a bulk packing fraction of approximately 0.1.

It should be noted that the highest packing fractions shown in Figure 13 and those used in the literature examples are quite large. For example, pure gaseous nitrogen at its normal boiling point of 77 K has a packing fraction of approximately 10^{-3}.

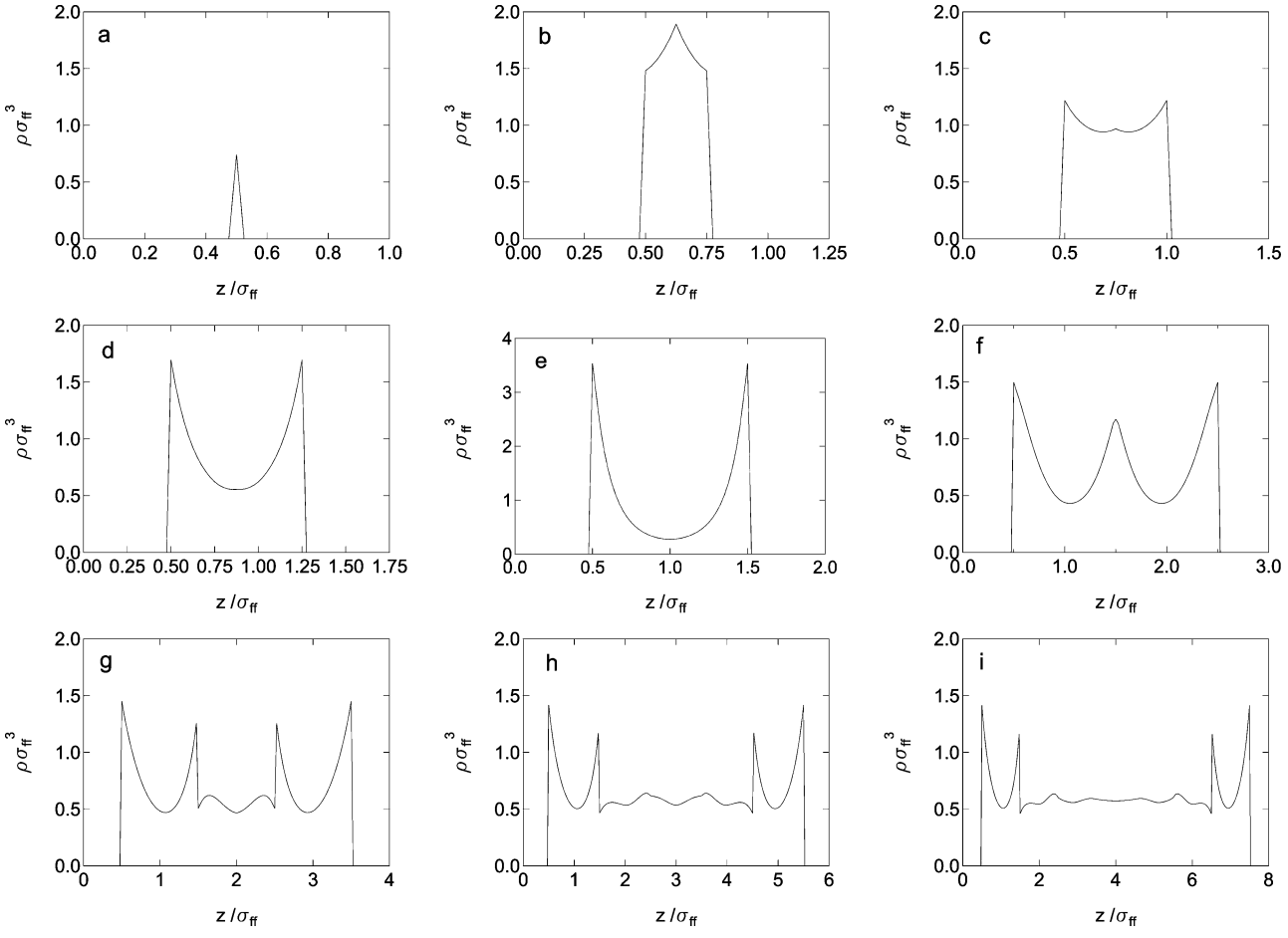

Figure 9. Attractive 3-mer against attractive SW walls at bulk packing fraction $\eta_b = 0.30$, which corresponds to $\rho\sigma_{ff}^3 = 0.57$. Pore widths are (a) $1\sigma_{ff}$, (b) $1.25\sigma_{ff}$, (c) $1.5\sigma_{ff}$, (d) $1.75\sigma_{ff}$, (e) $2\sigma_{ff}$, (f) $3\sigma_{ff}$, (g) $4\sigma_{ff}$, (h) $6\sigma_{ff}$, and (i) $8\sigma_{ff}$.

dx.doi.org/10.1021/jp406572d | J. Phys. Chem. C 2013, 117, 21337–21350

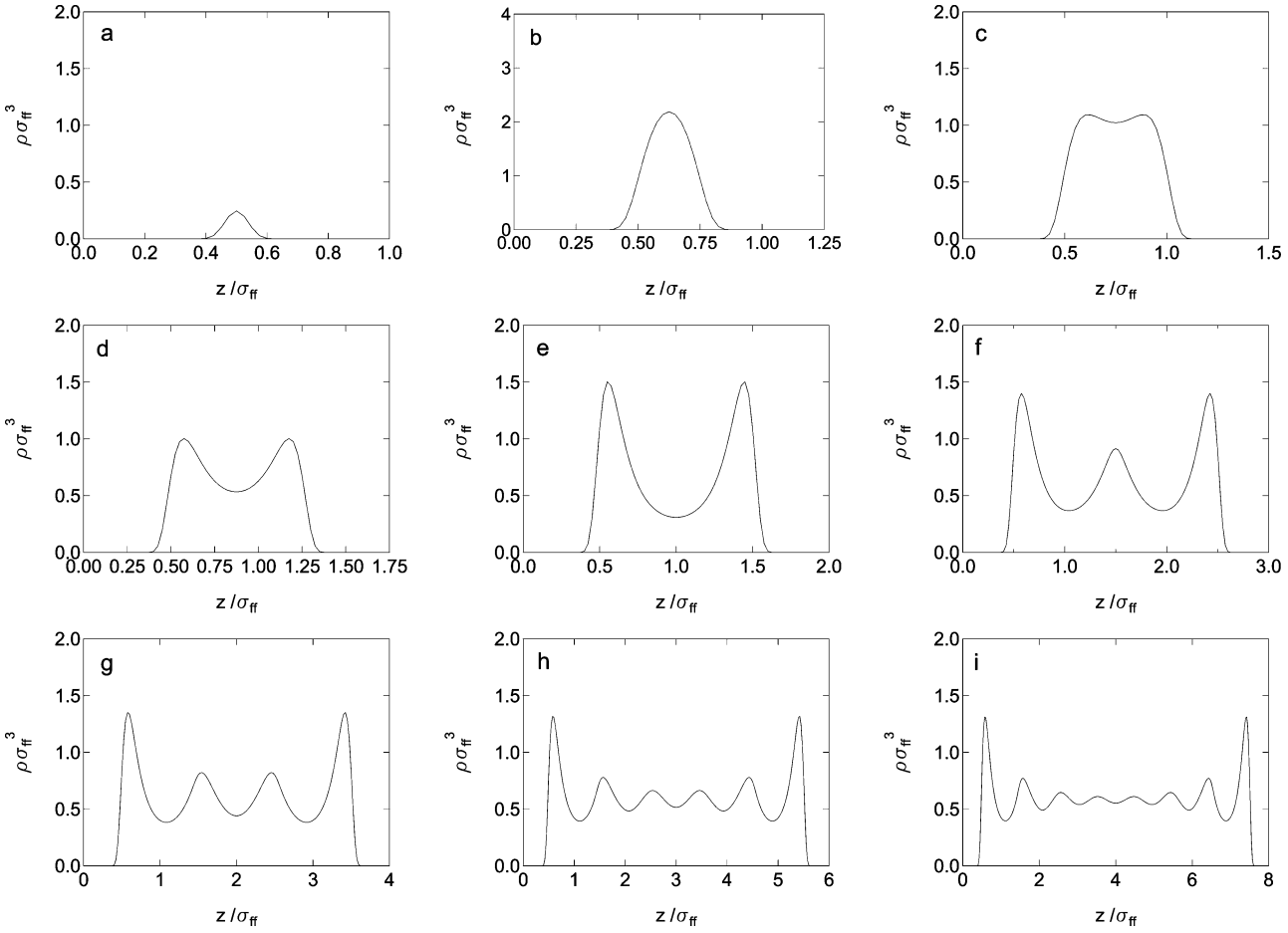

Figure 10. Attractive 3-mer against attractive LJ walls at bulk packing fraction $\eta_b = 0.30$, which corresponds to $\rho\sigma_{ff}^3 = 0.57$. Pore widths are (a) $1\sigma_{ff}$, (b) $1.25\sigma_{ff}$, (c) $1.5\sigma_{ff}$, (d) $1.75\sigma_{ff}$, (e) $2\sigma_{ff}$, (f) $3\sigma_{ff}$, (g) $4\sigma_{ff}$, (h) $6\sigma_{ff}$, and (i) $8\sigma_{ff}$.

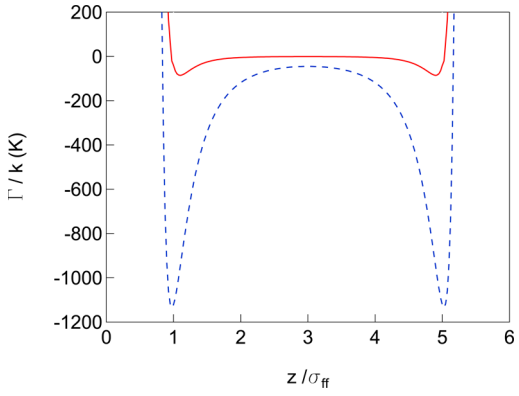

Figure 11. 6−12 Lennard-Jones and 10−4 wall potentials for attractive walls. Solid curve is 6−12 LJ potential, and dashed (- - -) curve is 10−4 potential.

Higher bulk packing fractions for gaseous nitrogen at 77 K would not be possible in an equilibrium sense, as it would condense to a liquid if pressure were increased.

4. CONCLUSIONS

A new implementation of density functional theory (DFT) has been developed to treat the adsorption of chain molecules on flat surfaces and in slit-shaped pores. A version of the statistical associating fluid theory (SAFT) based on the SAFT-VR equation provides the framework for the chemical potential in the bulk. Fundamental measure theory (FMT) was adopted to provide a rigorous description of the hard-sphere contribution to the free energy. By doing so, SAFT is transformed from a method for treatment of a homogeneous fluid in the bulk to an accurate method for analysis of an inhomogeneous fluid against a surface. The attractive term for adsorption using SAFT has been developed using a perturbation analysis out to second order, rather than by assuming a more approximate mean field.

Several systems involving the adsorption of *m*-mers have been considered. Calculations using the theory show excellent agreement with published Monte Carlo simulations for densities of hard sphere and hard-sphere chains of *m*-mers near a hard wall as well as a 3-mer with a square-well attractive potential near a hard wall or an attractive wall with a square-well potential. The FMT of Hansen-Goos and Roth,[14] which corresponds to a Carnahan−Starling−Boublík fluid, was found to be in better agreement with our hard-sphere simulations than the earlier FMT of Roth et al.,[13] which corresponds to a Mansoori−Carnahan−Starling−Leland fluid. Slit-shaped pores have been considered for adsorption of 3-mer chains using both square-well and Lennard−Jones wall potentials. Full slit pore density profiles for square-well and Lennard−Jones walls were compared and showed similar general behavior with differences attributable to the range of the potentials. To accommodate full slit-shaped pores, a 3-mer chain was modeled near walls with a 10−4 attractive potential. Surface excess adsorption isotherms

dx.doi.org/10.1021/jp406572d | J. Phys. Chem. C 2013, 117, 21337−21350

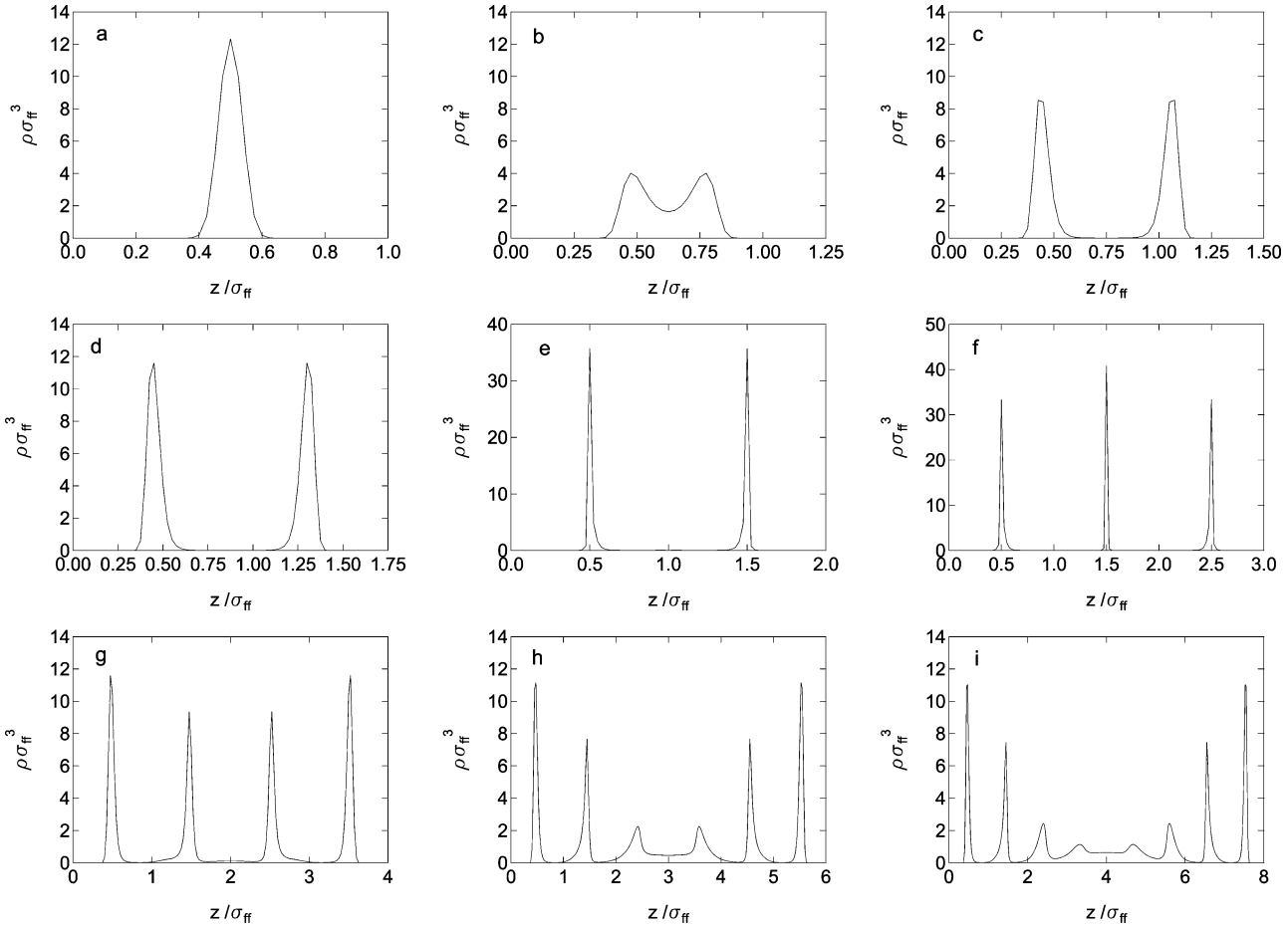

Figure 12. Attractive 3-mer in a pore with a 10−4 wall potential at a bulk packing fraction of $\eta_b = 0.30$, which corresponds to $\rho\sigma_{ff}^3 = 0.57$. Pore widths are (a) $1\sigma_{ff}$, (b) $1.25\sigma_{ff}$, (c) $1.5\sigma_{ff}$, (d) $1.75\sigma_{ff}$, (e) $2\sigma_{ff}$, (f) $3\sigma_{ff}$, (g) $4\sigma_{ff}$, (h) $6\sigma_{ff}$, and (i) $8\sigma_{ff}$.

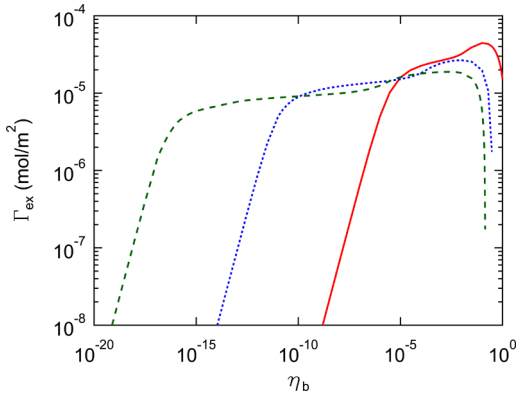

Figure 13. Surface excess isotherms inside a $4\sigma_{ff}$ pore at increasing bulk packing fractions for attractive 1-mer (solid), 2-mer (- - -), and 3-mer (– – –).

were determined for molecules of varying chain lengths inside such a pore.

The new theory should be useful for predicting adsorption on flat surfaces and in slit-shaped pores. A strength of the approach is the ability to compare predictions of the SAFT-based theory directly with simulation. While we have shown that the theory is in good agreement with the exact results obtained from the simulations for the molecular models studied, how well this approach will describe real fluids at high pressures has yet to be demonstrated. Nevertheless, the agreement between the predictions from the theory and the Monte Carlo simulations is encouraging for treatment of fluids in porous media at high pressures. The theory will be used to describe experimental results in future papers by the authors.

5. APPENDIX

Additional details on the development and implementation of the equation set are provided here.

5.1. DFT

For the hard-sphere contribution, the derivative of F_{hs} is

$$\frac{\delta F_{hs}[\rho(\mathbf{r})]}{\delta\rho(\mathbf{r})} = \int \sum_i \frac{\partial\Phi_{hs}}{\partial n_i(\mathbf{r})}\bigg|_{\mathbf{r}'} \frac{\delta n_i(\mathbf{r}')}{\delta\rho(\mathbf{r})} d\mathbf{r}' \tag{43}$$

The n_i terms for i = 2, 3, and $V2$ are developed from

$$n_2(z) = 2\pi R \int_{z-R}^{z+R} \rho(z')dz' \tag{44}$$

$$n_3(z) = \pi \int_{z-R}^{z+R} \rho(z')[R^2 - (z' - z)^2]dz' \tag{45}$$

$$\mathbf{n}_{V2}(z) = (-2\pi \int_{z-R}^{z+R} \rho(z')(z' - z)dz')\hat{\mathbf{z}} \equiv n_{V2}\hat{\mathbf{z}} \tag{46}$$

For the attractive terms, the derivatives of F_1 and F_2 are

dx.doi.org/10.1021/jp406572d | J. Phys. Chem. C 2013, 117, 21337−21350

$$\frac{\delta F_1[\rho(\mathbf{r})]}{\delta\rho(\mathbf{r})} = \int \rho(\mathbf{r}')g_{hs}[n_3(\mathbf{r}'');\,\mathbf{r}']\phi(|\mathbf{r}'-\mathbf{r}|) + \int\rho(\mathbf{r}')\int\rho(\mathbf{r}'')\frac{\delta g_{hs}[n_3(\mathbf{r}'');\,\mathbf{r}'']}{\delta\rho(\mathbf{r}'')}\phi(|\mathbf{r}'-\mathbf{r}''|)\mathrm{d}\mathbf{r}''\mathrm{d}\mathbf{r}' \quad (47)$$

$$\frac{\delta F_2[\rho(\mathbf{r})]}{\delta\rho(\mathbf{r})} = -\frac{1}{2kT}\int\rho(\mathbf{r}')(1+2\xi n_3{}^2) \times [\phi(|\mathbf{r}-\mathbf{r}'|)]^2 K_{hs}(\mathbf{r}')g_{hs}[n_3(\mathbf{r}');\,\mathbf{r}']\mathrm{d}\mathbf{r}' - \frac{1}{4kT}\int\rho(\mathbf{r}')\int\rho(\mathbf{r}'')[\phi(|\mathbf{r}'-\mathbf{r}''|)]^2\frac{\partial n_3}{\partial\rho} \times (4\xi n_3(\mathbf{r}'')K_{hs}(\mathbf{r}'')g_{hs}[n_3(\mathbf{r}'');\,\mathbf{r}''] + (1+2\xi n_3(\mathbf{r}''))\left[\frac{\partial K_{hs}(\mathbf{r}'')}{\partial n_3(\mathbf{r}'')}g_{hs}[n_3(\mathbf{r}'');\,\mathbf{r}''] + K_{hs}(\mathbf{r}'')\frac{\partial g_{hs}[n_3(\mathbf{r}'');\,\mathbf{r}'']}{\partial n_3(\mathbf{r}'')}\right]\mathrm{d}\mathbf{r}'\mathrm{d}\mathbf{r}'' \quad (48)$$

where $\xi = 1/\eta_{con}{}^2$. For the chain contribution, the derivative of F_{chain} is

$$\frac{\delta F_{chain}[\rho(\mathbf{r})]}{\delta\rho(\mathbf{r})} = \int\sum_i \frac{\partial\Phi_{chain}}{\partial n_i(\mathbf{r})}\bigg|_{\mathbf{r}'}\frac{\delta n_i(\mathbf{r}')}{\delta\rho(\mathbf{r})}\mathrm{d}\mathbf{r}' \quad (49)$$

The equation set was solved using a Picard iteration with Anderson mixing[81,82] and $\Delta z = R/40$.

5.2. Bulk Fluid

The chemical potential for the system is calculated using the following equations for a bulk fluid. There are two different densities, the molecular density $\rho_{m,b}$ and the segment density ρ_b, where $\rho_b = m\rho_{m,b}$. The chemical potential is calculated as the derivative of the Helmholtz free energy in the bulk, A, with respect to $\rho_{m,b}$, i.e.

$$\mu = \frac{\partial A}{\partial\rho_{m,b}} \quad (50)$$

where $A = A_{id} + A_{hs} + A_1 + A_2 + A_{chain}$. This gives for the ideal fluid

$$A_{id} = kT\rho_{m,b}[\ln(\Lambda^3\rho_{m,b}) - 1] \quad (51)$$

and yields eq 5. For the hard-sphere fluid, we have

$$A_{hs} = kT\sum_{i=0}^{3}\Phi_b^{hs}[n_{\alpha,b}(\mathbf{r})] \quad (52)$$

where $\Phi_b^{hs} = \Phi^{hs}[n_{\alpha,b}(\mathbf{r})]$. This gives eq 18. The first-order attractive potential, derived by Gil-Villegas et al.,[35] is described by

$$A_1 = -4\varepsilon(\lambda_f^3 - 1)n_{3,b}\rho_b g_e^{hs} \quad (53)$$

which gives eq 21. In contrast to the original SAFT-VR approach, the second-order attractive potential derived by Zhang[74] has been used and is given by

$$A_2 = -2\beta\varepsilon^2(\lambda_f^3 - 1)[\rho_b n_{3,b}(1+\xi n_{3,b}{}^2)K^{hs}g_e^{hs}] \quad (54)$$

which gives eq 27. The chain term of the Helmholtz free energy in the bulk is[61]

$$A_{chain} = kT\int\Phi_b^{chain}\mathrm{d}\mathbf{r} \quad (55)$$

where $\Phi_b^{chain} = \Phi^{chain}[n_{\alpha,b}(\mathbf{r})]$. Differentiation gives eq 32.

AUTHOR INFORMATION

Corresponding Author

*Phone: (615) 343-1672. Fax: (615) 343-7951. E-mail: m.douglas.levan@vanderbilt.edu.

Notes

The authors declare no competing financial interest.

REFERENCES

(1) Tarazona, P. Free-Energy Density Functional for Hard Spheres. *Phys. Rev. A* **1985**, *31*, 2672−2679; Erratum. *Phys. Rev. A* **1985**, *32*, 3148.

(2) Tarazona, P.; Marini Bettolo Marconi, U.; Evans, R. Phase Equilibria of Fluid Interfaces and Confined Fluids. Non-local Versus Local Density Functionals. *Mol. Phys.* **1987**, *60*, 573−595.

(3) Lastoskie, C.; Gubbins, K. E.; Quirke, N. Pore Size Distribution Analysis of Microporous Carbons: A Density Functional Theory Approach. *J. Phys. Chem.* **1993**, *97*, 4786−4796.

(4) Valladares, D. L.; Reinoso, F. R.; Zgrablich, G. Characterization of Active Carbons: The Influence of the Method in the Determination of the Pore Size Distribution. *Carbon* **1998**, *36*, 1491−1499.

(5) El-Merraoui, M.; Aoshima, M.; Kaneko, K. Micropore Size Distribution of Activated Carbon Fiber Using the Density Functional Theory and Other Methods. *Langmuir* **2000**, *16*, 4300−4304.

(6) Ravikovitch, P. I.; Vishnyakov, A.; Neimark, A. V. Density Functional Theories and Molecular Simulations of Adsorption and Phase Transitions in Nanopores. *Phys. Rev. E* **2001**, *64*, 011602.

(7) Ohba, T.; Nicholson, D.; Kaneko, K. Temperature Dependence of Micropore Filling of N_2 in Slit-Shaped Carbon Micropores: Experiment and Grand Canonical Monte Carlo Simulation. *Langmuir* **2003**, *19*, 5700−5707.

(8) Jagiello, J.; Thommes, M. Comparison of DFT Characterization Methods Based on N_2, Ar, CO_2, and H_2 Adsorption Applied to Carbons with Various Pore Size Distributions. *Carbon* **2004**, *42*, 1227−1232.

(9) Nguyen, T. X.; Bhatia, S. K. Probing the Pore Wall Structure of Nanoporous Carbons Using Adsorption. *Langmuir* **2004**, *20*, 3532−3535.

(10) Ustinov, E. A.; Do, D. D. Application of Density Functional Theory to Analysis of Energetic Heterogeneity and Pore Size Distribution of Activated Carbon. *Langmuir* **2004**, *20*, 3791−3797.

(11) Rosenfeld, Y. Free-Energy Model for the Inhomogeneous Hard-Sphere Fluid Mixture and Density-Functional Theory of Freezing. *Phys. Rev. Lett.* **1989**, *63*, 980−983.

(12) Rosenfeld, Y.; Schmidt, M.; Lowen, H.; Tarazona, P. Fundamental-Measure Free-Energy Density Functional for Hard Spheres: Dimensional Crossover and Freezing. *Phys. Rev. E* **1997**, *55*, 4245−4263.

(13) Roth, R.; Evans, R.; Lang, A.; Kahl, G. Fundamental Measure Theory for Hard-Sphere Mixtures Revisited: the White Bear Version. *J. Phys.: Condens. Matter* **2002**, *14*, 12063−12078.

(14) Hansen-Goos, H.; Roth, R. Density Functional Theory for Hard Sphere Mixtures: the White Bear Version Mark II. *J. Phys.: Condens. Matter* **2006**, *18*, 8413−8425.

(15) Roth, R. Fundamental Measure Theory for Hard-Sphere Mixtures: A Review. *J. Phys.: Condens. Matter* **2010**, *22*, 063102.

(16) Bryk, P.; Roth, R.; Mecke, K. R.; Dietrich, S. Hard-Sphere Fluids in Contact with Curved Substrates. *Phys. Rev. E* **2003**, *68*, 031602.

(17) Figueroa-Gerstenmaier, S.; Blas, F. J.; Avalos, J. B.; Vega, L. F. Application of the Fundamental Measure Density Functional Theory to the Adsorption in Cylindrical Pores. *J. Chem. Phys.* **2003**, *118*, 830−842.

(18) Kierlik, E.; Rosinberg, M. L.; Fan, Y.; Monson, P. A. Prewetting at a Liquid Mixture-Solid Interface: A Comparison of Monte Carlo

Simulations with Mean Field Density Functional Theory. *J. Chem. Phys.* **1994**, *101*, 10947−10952.
(19) Malijevsky, A. Fundamental Measure Theory in Cylindrical Geometry. *J. Chem. Phys.* **2007**, *126*, 134710.
(20) Evans, R. *Fundamentals of Inhomogeneous Fluids*; Marcel Dekker: New York, 1992.
(21) Evans, R. *Density Functional Theory for Inhomogeneous Fluids I: Simple Fluids in Equilibrium*; 3rd Warsaw School of Statistical Physics: Warsaw University Press: Warsaw, 2010.
(22) Wertheim, M. S. Fluids with Highly Directional Attractive Forces. I. Statistical Thermodynamics. *J. Stat. Phys.* **1984**, *35*, 19−34.
(23) Wertheim, M. S. Fluids with Highly Directional Attractive Forces. II. Thermodynamic Perturbation Theory and Integral Equations. *J. Stat. Phys.* **1984**, *35*, 35−47.
(24) Wertheim, M. S. Fluids with Highly Directional Attractive Forces. III. Multiple Attraction Sites. *J. Stat. Phys.* **1986**, *42*, 459−476.
(25) Wertheim, M. S. Fluids with Highly Directional Attractive Forces. IV. Equilibrium Polymerization. *J. Stat. Phys.* **1986**, *42*, 477−492.
(26) McCabe, C.; Galindo, A.; Gil-Villegas, A.; Jackson, G. Predicting the High-Pressure Phase Equilibria of Binary Mixtures of n-Alkanes Using the SAFT-VR Approach. *Int. J. Thermophys.* **1998**, *19*, 1511−1522.
(27) McCabe, C.; Gil-Villegas, A.; Jackson, G. Predicting the High-Pressure Phase Equilibria of Methane + n-Hexane Using the SAFT-VR Approach. *J. Phys. Chem. B* **1998**, *102*, 4183−4188.
(28) McCabe, C.; Galindo, A.; Gil-Villegas, A.; Jackson, G. Predicting the High-Pressure Phase Equilibria of Binary Mixtures of Perfluoro-n-Alkanes Plus n-Alkanes Using the SAFT-VR Approach. *J. Phys. Chem. B* **1998**, *102*, 8060−8069.
(29) Galindo, A.; Gil-Villegas, A.; Whitehead, P. J.; Jackson, G.; Burgess, A. N. Prediction of Phase Equilibria for Refrigerant Mixtures of Difluoromethane (HFC-32), 1,1,1,2-Tetrafluoroethane (HFC-134a), and Pentafluoroethane (HFC-125a) Using SAFT-VR. *J. Phys. Chem. B* **1998**, *102*, 7632−7639.
(30) Jackson, G.; Chapman, W. G.; Gubbins, K. E. Phase Equilibria of Associating Fluids: Spherical Molecules with Multiple Bonding Sites. *Mol. Phys.* **1988**, *65*, 1−31.
(31) Chapman, W. G.; Jackson, G.; Gubbins, K. E. Phase Equilibria of Associating Fluids: Chain Molecules with Multiple Bonding Sites. *Mol. Phys.* **1988**, *65*, 1057−1079.
(32) Huong, S. H.; Radosz, M. Equation of State for Small, Large, Polydisperse, and Associating Molecules. *Ind. Eng. Chem. Res.* **1990**, *29*, 2284−2294.
(33) Johnson, J. K.; Muller, E. A.; Gubbins, K. E. Equation of State for Lennard-Jones Chains. *J. Phys. Chem.* **1994**, *98*, 6413−6419.
(34) Blas, F. J.; Vega, L. F. Thermodynamic Behaviour of Homonuclear and Heteronuclear Lennard-Jones Chains with Association Sites from Simulation and Theory. *Mol. Phys.* **1997**, *92*, 135−150.
(35) Gil-Villegas, A.; Galindo, A.; Whitehead, P. J.; Mills, S. J.; Jackson, G.; Burgess, A. N. Statistical Associating Fluid Theory for Chain Molecules with Attractive Potentials of Variable Range. *J. Chem. Phys.* **1997**, *106*, 4168−4186.
(36) Gross, J.; Sadowski, G. Perturbed-Chain SAFT: An Equation of State Based on a Perturbation Theory for Chain Molecules. *Ind. Eng. Chem. Res.* **2001**, *40*, 1244−1260.
(37) Pedrosa, N.; Vega, L. F.; Coutinho, J. A. P.; Marrucho, I. M. Phase Equilibria Calculations of Polyethylene Solutions from SAFT-Type Equations of State. *Macromolecules* **2006**, *39*, 4240−4246.
(38) Watson, G.; Lafitte, T.; Zeberg-Mikkelsen, C. K.; Baylaucq, A.; Bessieres, D.; Boned, C. Volumetric and Derivative Properties Under Pressure for the System 1-Propanol Plus Toluene: A Discussion of PC-SAFT and SAFT-VR. *Fluid Phase Equilib.* **2006**, *247*, 121−134.
(39) Haslam, A. J.; von Solms, N.; Adjiman, C. S.; Galindo, A.; Jackson, G.; Paricaud, P.; Michelsen, M. L.; Kontogeorgis, G. M. Predicting Enhanced Absorption of Light Gases in Polyethylene Using Simplified PC-SAFT and SAFT-VR. *Fluid Phase Equilib.* **2006**, *243*, 74−91.
(40) Watson, G.; Lafitte, T.; Zeberg-Mikkelsen, C. K.; Baylaucq, A.; Bessieres, D.; Boned, C. Volumetric and Derivative Properties Under Pressure for the System 1-Propanol Plus Toluene: A Discussion of PC-SAFT and SAFT-VR *Fluid Phase Equilib.* 2006, *247*, 121−134. Erratum. *Fluid Phase Equilib.* **2007**, *253*, 80.
(41) Castro-Marcano, F.; Olivera-Fuentes, C. G.; Colina, C. M. Joule-Thomson Inversion Curves and Third Virial Coefficients for Pure Fluids from Molecular-Based Models. *Ind. Eng. Chem. Res.* **2008**, *47*, 8894−8905.
(42) Courtial, X.; Soo, C. B.; Coquelet, C.; Paricaud, P.; Ramjugernath, D.; Richon, D. Vapor-Liquid Equilibrium in the n-Butane Plus Methanol System, Measurement and Modeling from 323.2 to 443.2 K. *Fluid Phase Equilib.* **2009**, *277*, 152−161.
(43) McCabe, C.; Galindo, A. SAFT Associating Fluids and Fluid Mixtures. In *Applied Thermodynamics of Fluids*; Goodwin, A. R. H., Sengers, J. V., Peters, C. J., Eds.; Royal Society of Chemistry: London, 2010.
(44) Zhao, H. G.; McCabe, C. Phase Behavior of Dipolar Fluids from a Modified Statistical Associating Fluid Theory for Potentials of Variable Range. *J. Chem. Phys.* **2006**, *125*, 4504−4515.
(45) Zhao, H. G.; dos Ramos, M. C.; McCabe, C. Development of an Equation of State for Electrolyte Solutions by Combining the Statistical Associating Fluid Theory and the Mean Spherical Approximation for the Nonprimitive Model. *J. Chem. Phys.* **2007**, *126*, 244503.
(46) Zhao, H. G.; Ding, Y.; McCabe, C. Phase Behavior of Dipolar Associating Fluids from the SAFT-VR+D Equation of State. *J. Chem. Phys.* **2007**, *127*, 084514.
(47) Lymperiadis, A.; Adjiman, C. S.; Galindo, A.; Jackson, G. A Group Contribution Method for Associating Chain Molecules Based on the Statistical Associating Fluid Theory (SAFT-gamma). *J. Chem. Phys.* **2007**, *127*, 234903.
(48) McCabe, C.; Jackson, G. SAFT-VR Modelling of the Phase Equilibrium of Long-Chain n-Alkanes. *Phys. Chem. Chem. Phys.* **1999**, *1*, 2057−2064.
(49) McCabe, C.; Galindo, A.; Garcia-Lisbona, M. N. Examining the Adsorption (Vapor-Liquid Equilibria) of Short-Chain Hydrocarbons in Low-Density Polyethylene with the SAFT-VR Approach. *Ind. Eng. Chem. Res.* **2001**, *40*, 3835−3842.
(50) Paricaud, P.; Galindo, A.; Jackson, G. Modeling the Cloud Curves and the Solubility of Gases in Amorphous and Semicrystalline Polyethylene with the SAFT-VR Approach and Flory Theory of Crystallization. *Ind. Eng. Chem. Res.* **2004**, *43*, 6871−6889.
(51) Yethiraj, A.; Woodward, C. E. Monte Carlo Density Functional Theory of Nonuniform Polymer Melts. *J. Chem. Phys.* **1995**, *102*, 5499−5505.
(52) Forsman, J.; Woodward, C. E. An Improved Density Functional Description of Hard Sphere Polymer Fluids at Low Density. *J. Chem. Phys.* **2003**, *119*, 1889−1892.
(53) Blas, F. J.; del Rio, E. M.; de Miguel, E.; Jackson, G. An Examination of the Vapour-Liquid Interface of Associating Fluids Using a SAFT-DFT Approach. *Mol. Phys.* **2001**, *99*, 1851−1865.
(54) Gloor, G. J.; Blas, F. J.; del Rio, E. M.; de Miguel, E.; Jackson, G. A SAFT-DFT Approach for the Vapour-Liquid Interface of Associating Fluids. *Fluid Phase Equilib.* **2002**, *194*, 521−530.
(55) Gloor, G. J.; Jackson, G.; Blas, F. J.; del Rio, E. M.; de Miguel, E. An Accurate Density Functional Theory for the Vapor-Liquid Interface of Associating Chain Molecules Based on the Statistical Associating Fluid Theory for Potentials of Variable Range. *J. Chem. Phys.* **2004**, *121*, 12740−12759.
(56) Gloor, G. J.; Jackson, G.; Blas, F. J.; del Rio, E. M.; de Miguel, E. Prediction of the Vapor-Liquid Interfacial Tension of Nonassociating and Associating Fluids with the SAFT-VR Density Functional Theory. *J. Chem. Phys.* **2007**, *111*, 15513−15522.
(57) Georgiadis, A.; Llovell, F.; Bismarck, A.; Blas, F. J.; Galindo, A.; Maitland, G. C.; Trusler, J. P. M.; Jackson, G. Interfacial Tension Measurements and Modelling of (Carbon Dioxide Plus n-Alkane) and (Carbon Dioxide Plus Water) Binary Mixtures at Elevated Pressures and Temperatures. *J. Supercrit. Fluids* **2010**, *55*, 743−754.

(58) Llovell, F.; Galindo, A.; Blas, F. J.; Jackson, G. Classical Density Functional Theory for the Prediction of the Surface Tension and Interfacial Properties of Fluids Mixtures of Chain Molecules Based on the Statistical Associating Fluid Theory for Potentials of Variable Range. *J. Chem. Phys.* **2010**, *133*, 024704.
(59) Llovell, F.; MacDowell, N.; Galindo, A.; Blas, F. J.; Jackson, G. Application of the SAFT-VR Density Functional Theory to the Prediction of the Interfacial Properties of Mixtures of Relevance to Reservoir Engineering. *Fluid Phase Equilib.* **2012**, *336*, 137−150.
(60) Yu, Y. X.; Wu, J. Z. A Fundamental-Measure Theory for Inhomogeneous Associating Fluids. *J. Chem. Phys.* **2002**, *116*, 7094−7103.
(61) Yu, Y. X.; Wu, J. Z. Density Functional Theory for Inhomogeneous Mixtures of Polymeric Fluids. *J. Chem. Phys.* **2002**, *117*, 2368−2376.
(62) Yu, Y. X.; Wu, J. Z.; Xin, Y. X.; Gao, G. H. Structures and Correlation Functions of Multicomponent and Polydisperse Hard-Sphere Mixtures from a Density Functional Theory. *J. Chem. Phys.* **2004**, *121*, 1535−1541.
(63) Bryk, P.; Sokolowski, S.; Pizio, O. Density Functional Theory for Inhomogeneous Associating Chain Fluids. *J. Chem. Phys.* **2006**, *125*, 024909.
(64) Ye, Z. C.; Cai, J.; Liu, H. L.; Hu, Y. Density and Chain Conformation Profiles of Square-Well Chains Confined in a Slit by Density-Functional Theory. *J. Chem. Phys.* **2005**, *123*, 194902.
(65) Ye, Z. C.; Chen, H. Y.; Liu, H. L.; Hu, Y.; Jiang, J. W. Density Functional Theory for Copolymers Confined in a Nanoslit. *J. Chem. Phys.* **2007**, *126*, 134903.
(66) Tripathi, S.; Chapman, W. G. Microstructure of Inhomogeneous Polyatomic Mixtures from a Density Functional Formalism for Atomic Mixtures. *J. Chem. Phys.* **2005**, *122*, 094506.
(67) Jain, S.; Dominik, A.; Chapman, W. G. Modified Interfacial Statistical Associating Fluid Theory: A Perturbation Density Functional Theory for Inhomogeneous Complex Fluids. *J. Chem. Phys.* **2007**, *127*, 244904.
(68) Carnahan, N. F.; Starling, K. E. Equation of State for Nonattracting Rigid Spheres. *J. Chem. Phys.* **1969**, *51*, 635−636.
(69) Chang, J.; Sandler, S. I. A Real Functional Representation for the Structure of the Hard-Sphere Fluid. *Mol. Phys.* **1994**, *81*, 735−744.
(70) Verlet, L.; Weis, J. J. Equilibrium Theory of Simple Liquids. *Phys. Rev. A* **1972**, *5*, 939−952.
(71) Patel, B. H.; Docherty, H.; Varga, S.; Galindo, A.; Maitland, G. C. Generalized Equation of State for Square-Well Potentials of Variable Range. *Mol. Phys.* **2005**, *103*, 129−139.
(72) Barker, J. A.; Henderson, D. Pertubation Theory and Equation of State for Fluids: The Square-Well Fluid. *J. Chem. Phys.* **1967**, *47*, 2856−2861.
(73) Barker, J. A.; Henderson, D. What is "Liquid"? Understanding the States of Matter. *Rev. Mod. Phys.* **1976**, *48*, 587−671.
(74) Zhang, B. J. Calculating Thermodynamic Properties from Perturbation Theory II. An Analytical Representation of Square-Well Chain Fluid. *Fluid Phase Equilib.* **2001**, *180*, 182−194.
(75) Prausnitz, J. M.; Lichtenthaler, R. N.; de Azevedo, E. G. *Molecular Thermodynamics of Fluid-Phase Equilibria*, 3rd ed.; Prentice Hall: NJ, 1999.
(76) Steele, W. A. The Physical Interaction of Gases with Crystalline Solids. I. Gas-Solid Energies and Properties of Isolated Adsorbed Atoms. *Surf. Sci.* **1973**, *36*, 317−352.
(77) Tjatjopoulos, G. J.; Feke, D. L.; Mann, J. A. Molecule-Micropore Interaction Potentials. *J. Phys. Chem.* **1988**, *92*, 4006−4007.
(78) Snook, I. K.; Henderson, D. Monte Carlo Study of a Hard-Sphere Fluid Near a Hard Wall. *J. Chem. Phys.* **1978**, *68*, 2134−2139.
(79) Kierlik, E.; Rosinberg, M. L. Perturbation Density Functional Theory for Polyatomic Fluids. III. Applications to Hard Chain Molecules in Slitlike Pores. *J. Chem. Phys.* **1978**, *100*, 1716−30.
(80) Dickman, R.; Hall, C. K. High Density Monte Carlo Simulations of Chain Molecules: Bulk Equation of State and Density Profiles Near Walls. *J. Chem. Phys.* **1988**, *89*, 3168−3174.
(81) Anderson, D. G. Iterative Procedures for Nonlinear Integral Equations. *J. Assoc. Comput. Mach.* **1965**, *12*, 547−560.
(82) Eyert, V. A Comparative Study of Methods for Convergence Acceleration of Iterative Vector Sequences. *J. Comput. Phys.* **1996**, *124*, 271−285.